Classification of Atlantic Coastal Sand Dune Vegetation Using In Situ, UAV, and Airborne Hyperspectral Data

Quentin Laporte-Fauret, Bertrand Lubac, Bruno Castelle, Richard Michalet, Vincent Marieu, Lionel Bombrun, Patrick Launeau, Manuel Giraud, Cassandra Normandin, David Rosebery

remote sensing

MDPI

Article

Classification of Atlantic Coastal Sand Dune Vegetation Using In Situ, UAV, and Airborne Hyperspectral Data

Quentin Laporte-Fauret [1,*], Bertrand Lubac [1], Bruno Castelle [1], Richard Michalet [1], Vincent Marieu [1], Lionel Bombrun [2], Patrick Launeau [3], Manuel Giraud [3], Cassandra Normandin [1] and David Rosebery [4]

1 University of Bordeaux, CNRS, UMR 5805 EPOC, Allée Geoffroy Saint-Hilaire, 33615 Pessac CEDEX, France; bertrand.lubac@u-bordeaux.fr (B.L.); bruno.castelle@u-bordeaux.fr (B.C.); richard.michalet@u-bordeaux.fr (R.M.); vincent.marieu@u-bordeaux.fr (V.M.); cassandra.normandin@gmail.com (C.N.)

2 University of Bordeaux, CNRS, UMR 5218 IMS, Cours de la libération, 33405 Talence CEDEX, France; lionel.bombrun@agro-bordeaux.fr

3 University of Nantes, CNRS, UMR 6112 LPG, Rue de la Houssinière, 42322 Nantes, France; patrick.launeau@univ-nantes.fr (P.L.); manuel.giraud@univ-nantes.fr (M.G.)

4 Office National des Forêts, 9 rue R Manaud, 33524 Bruges, France; david.rosebery@onf.fr

* Correspondence: quentin.laporte-fauret@u-bordeaux.fr; Tel.: +33-540-003-316

Received: 10 June 2020; Accepted: 9 July 2020; Published: 11 July 2020

Abstract: Mapping coastal dune vegetation is critical to understand dune mobility and resilience in the context of climate change, sea level rise, and increased anthropogenic pressure. However, the identification of plant species from remotely sensed data is tedious and limited to broad vegetation communities, while such environments are dominated by fragmented and small-scale landscape patterns. In June 2019, a comprehensive multi-scale survey including unmanned aerial vehicle (UAV), hyperspectral ground, and airborne data was conducted along approximately 20 km of a coastal dune system in southwest France. The objective was to generate an accurate mapping of the main sediment and plant species ground cover types in order to characterize the spatial distribution of coastal dune stability patterns. Field and UAV data were used to assess the quality of airborne data and generate a robust end-member spectral library. Next, a two-step classification approach, based on the normalized difference vegetation index and Random Forest classifier, was developed. Results show high performances with an overall accuracy of 100% and 92.5% for sand and vegetation ground cover types, respectively. Finally, a coastal dune stability index was computed across the entire study site. Different stability patterns were clearly identified along the coast, highlighting for the first time the high potential of this methodology to support coastal dune management.

Keywords: airborne hyperspectral; coastal dune vegetation; end-member spectral library; pixel-based supervised classification; Random Forest; stability index

1. Introduction

The formation and evolution of coastal sand dunes, which back sandy beaches, result from complex interactions between marine and aeolian sediment transport, plant ecosystem-engineering effects, coastal and beach topography, and storms [1–7]. When not destroyed by human activity, foredunes are formed by an accumulation of wind-blown sand, which is trapped by plant species tolerant to sand burial. Indeed, once pioneer species that are tolerant to salinity and sand burial colonize a shoreline, a positive feedback occurs between the trapped sand settling and the pioneer

species colonization leading to the construction of the foredune [6]. This foredune provides a shelter, reducing landward sand transport, and favors the colonization of vegetation species that are not tolerant to sand burial, promoting plant succession, and, thus, an increase in vegetation cover and stabilization of the dune system [8–10]. In addition, vegetated coastal dunes provide many other ecosystem services, acting as a natural and effective barrier against marine flooding and storm waves and greatly enhancing beach resilience [11], plant ecological niches, pollutant filtration, or nesting sites [12]. However, the development of tourist activities in these environments can lead to a strong degradation of the ecosystem and of the beach-dune system [12]. As dunes play an important role in the protection from waves and flooding during storms by acting as a natural barrier, in recent decades, many management plans have been proposed to prevent erosion and promote dune stabilization at the detriment of natural processes. These management strategies generally include beach nourishment [13], vegetation planting [14], sand fencing [15], or mechanical reprofiling [16]. Recently, in some regions of the world, this method of stabilization has been challenged by another method that encourages the dynamism of the environment in order to restore dune diversity and mobility [17–19]. Indeed, coastal dune vegetation can affect the vulnerability of coastlines by determining the maximum height of the foredune, but also their resilience, by modifying sand mobility [20,21]. Therefore, coastal dunes play a crucial role for the future of sandy coasts [21,22]. In this context, mapping and monitoring the spatial and temporal distribution of plant communities, together with morphological changes, is critical to improve our understanding of coastal dune changes in response to natural forcing. This is crucial for management strategies, ultimately for designing optimal sustainable development of these systems.

During the last few decades, multispectral and hyperspectral optical imagery showed high potential to characterize spatial and temporal dynamics of coastal vegetation [23–25]. When combined with exogenous data, these methods can answer ecological [26] and geomorphological [27] questions across a wide range of scales. While airborne-based hyperspectral applications attempted to discriminate vegetation at the species level, satellite-based multispectral approaches were mainly limited to the identification of broad vegetation communities in fine-scale (1 m) and complex mosaic landscapes [23]. Because of reduced costs and time efforts, recent developments mainly focus on multispectral approaches. They attempt to address and partially overcome the species detection limitation using increased sensor capacities and methodological advances. For instance, based on phenological features derived from multiyear time series of satellite images, phenology-based mapping approaches allow us to address low biomass and highly fragmented systems [24]. Hybrid pixel-based and object-oriented approaches using spectral and textural information at high [28,29] and very-high [25] resolutions demonstrate a high potential for discrimination of plant species and fine scale interspersed coastal plant communities.

However, despite these improved performances, hyperspectral applications still provide higher classification accuracies at species level than multispectral approaches [30]. In the past years, a lot of effort was dedicated to the development and comparison of different classifiers [31,32]. However, few studies focused on the methodology to generate ab end-member spectral library [27,29], which is a key issue to increase performances and provide automated and repeatable methods [33,34].

Our main objective in this study is to produce an accurate mapping of a large number of ground cover types, including sediment, individual plant species, and broad plant communities, using an original two-step pixel-based classification approach. This approach, based on a normalized difference vegetation index (NDVI) and Random Forest classifier (RF), was developed from a comprehensive dataset composed of an unmanned aerial vehicle (UAV), hyperspectral ground, and airborne data. In addition, we also aim to examine the spatial distribution of sediment and vegetation in order to characterize coastal dune stability patterns that are important from the perspective of sustainable coastal dune management.

2. Study Area

The study site is composed of beach-dune systems extending approximately 18 km alongshore in Aquitaine, southwest France, from the Horizon beach to Grand Crohot beach (Figure 1a). This preserved area, which is characterized by the absence of coastal resort and hard structures, represents an ideal natural laboratory that has been used for assessing beach-dune evolution [35,36], plant–plant interactions, and community composition [37–40]. Beaches are meso-macrotidal with a mean annual spring tide of 3.7 m [41]. The coast is exposed to high-energy waves generated in the North Atlantic Ocean. Winter wave energy shows large interannual variability, which can lead to dramatic coastal dune erosion during severe winters [41,42]. Contrary to further north along the coast, where chronic erosion can reach 5 m/y, the shoreline at the study area has been relatively stable over the past 65 years [43,44]. The large aeolian sand dunes have been formed through a mixture of natural Aeolian and biological processes and large-scale anthropogenic works, primarily [45]: (1) erection of a foredune by progressive fencing at the end of the 19th century and (2) extensive dune reprofiling with large-scale mechanical aid and marram planting [46,47]. Since then, the coastal dune system has been softly managed by marram grass planting and branching, particularly to prevent the development of blowouts. Current coastal dune height reaches 20 to 25 m above mean sea level, with a width of approximatively 250 m, and is composed, from the sea to the inland, of (1) the incipient foredune formed by Aeolian sand deposition; (2) the established foredune, a shore-parallel dune ridge formed on the backshore by Aeolian sand deposition and vegetation; (3) the transition dune; and (4) the grey dune, occupying the most inland position closest to the forest. Vegetation zonation follows these four morphological units in relation to plant species tolerance to physical disturbance (erosion and accretion due to marine and wind activity) (Figure 1b) [4,37].

The incipient foredune (the most disturbed unit subject to marine and Aeolian action) is mainly colonized by *Elymus farctus* (Ely, Figure 1c). This pioneer species can rapidly grow in this habitat because of its high tolerance to sand deposition and the increase in sediment fertility provided by organic matter brought by the sea and the decrease in atmospheric stress due to the water spray [37]. The associated pioneer species (*Euphorbia paralias* and *Eryngium maritimum*, Figure 1c) mainly form diffuse patches with low vegetation cover (<30%) [37].

The established foredune (a less disturbed unit mainly subject to Aeolian action) is largely dominated by *Ammophila arenaria* (Amm, Figure 1c), a species which was used for dune building due to its long leaves, which trap the windblown sand and its dense root network promoting dune stabilization. The plantation of *Ammophila arenaria* is still used nowadays by coastal dune stakeholders for promoting dune recovery after severe winter storms. Other species are *Otanthus maritimus* (Ota, Figure 1c), generally pure low-density patches on the established foredune ocean face, and *Galium arenarium* (Gal, Figure 1c), forming dense patches of several tens of meters on the established foredune inland face when fully developed at the end of spring. The incipient foredune (IFS) and established foredune (EFS) sands are both characterized by a highly mobile surface sand (for mobile dune sand (MDS)), with a median grain size of 414 μm [40].

Behind the established foredune is the transition dune (more stable and less subject to sand burial), colonized by perennial species, primarily *Helychrisum stoechas* (Hel, Figure 1c) and *Artemisia campestris* (Art, Figure 1c), the latter developing dense patches extending a few meters horizontally. Here, the grains of sand are slightly finer (median grain size of 389 μm [40]) and are mixed with plant debris (grey dune sand (GDS)).

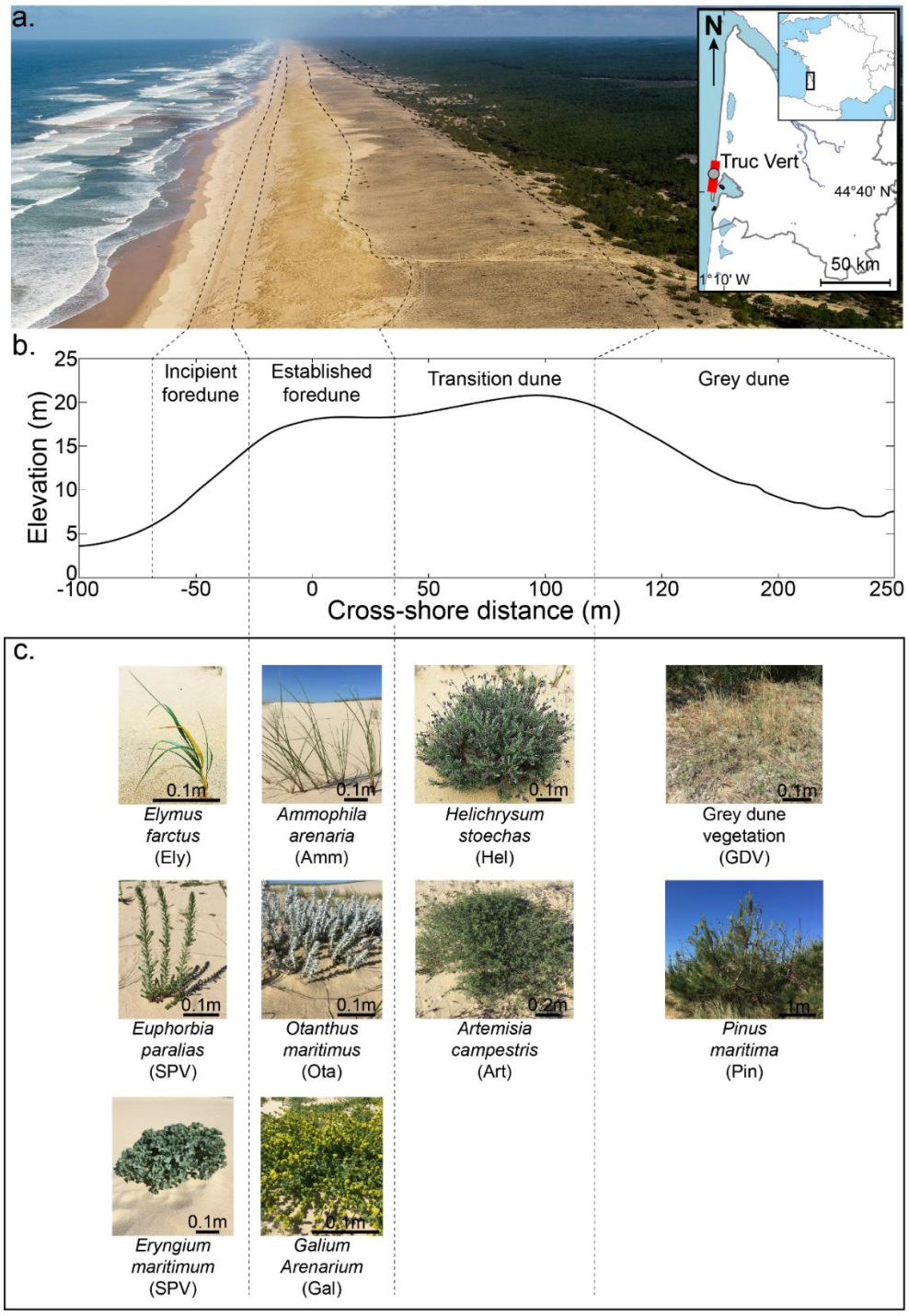

Figure 1. (**a**) Location map and aerial photograph of Truc Vert beach, representative of southwest France beaches with a well-managed alongshore-uniform coastal dune; the red line on the location map indicates the 18 km of coastline studied; (**b**) cross-shore profile of the Truc Vert beach/dune system, showing the different coastal dune units; and (**c**) photographs of the dominant coastal dune plant species.

Finally, the grey dune (highly stable and mostly sheltered from sand sprinkling during winter storms) is at the junction between the herbaceous and forest environments. It is characterized by the presence of mosses, lichens, the perennial grass *Corynephorus canescens*, many small annuals (*Phleum arenarium*, *Cerastium glomeratum*, *Vulpia membranacea*, and *Senecio vulgaris*), and woody species such as *Pinus maritima* (Pin, Figure 1c). In addition, it is an environment of high floristic interest,

which is classified as a priority natural habitat by the European commission (Habitat Code 2130 in the Habitat Directive 62/43 (of 21 May 1992, applicable in France since 1994)).

Plant species and natural habitats previously described allow us to define 11 plant communities and sand cover classes (Amm, Gal, Hel, Art, Ely, Ota, MDS, GDS, sparse vegetation (SPV), grey dune vegetation (GDV), Pin, see Table 1), which, for the most part, play a major role in the morphological and ecological processes of the coastal dunes in southwest France [37]. SPV (i.e., SParse vegetation, Figure 1c) gathers some species of the incipient foredune (i.e., *Euphorbia paralias* and *Eryngium maritimum*), which cannot be radiometrically discriminated between them with a 1 m^2 resolution sensor due to the very low coverage and very small scale of features. For the same reasons, grey dune vegetation (GDV; Figure 1c) gathers some species of the grey dune (i.e., *Corynephorus canescens*, *Phleum arenarium*, *Cerastium glomeratum*, *Vulpia membranacea*, and *Senecio vulgaris*). These species are interspersed with each other in very dense features. The eastern boundary of the study site is defined by the iso-contour of topographic elevation z = 12 m, which corresponds to the middle of the grey dune inland face. The western boundary is defined as the beach—incipient foredune limit monitored on 21 May 2019 using an all-terrain vehicle (ATV), equipped with a differential global positioning system (DGPS).

Table 1. Sampling strategies and the number of collected points for the different plant species and sand types. The choice of the sampling strategy depends on the patch size (large patch ≥1 m^2; small patch <1 m^2; very small patch <<1 m^2), optical homogeneity, and species diversity in a 1 × 1 m^2 pixel. List of acronyms: Amm (*Ammophila arenaria*), Gal (*Galium arenarium*), Hel (*Helychrisum stoechas*), Art (*Artemisia campestris*), Ely (*Elymus farctus*), Ota (*Otanthus maritimus*), MDS (Mobile Dune Sand), GDS (Grey Dune Sand), SPV (Sparse Vegetation), GDV (Grey Dune Vegetation), Pin (*Pinus marimima*), IFS (Incipient Foredune Sand), EFS (Established Foredune Sand).

Classes	Characteristics of Ground Covers	Sampling Strategy	# Collected Replicates
Amm	Large patches	Field 9 points/quadra	90
Gal	Large patches	Field 9 points/quadra	90
Hel	Large patches	Field 9 points/quadra	90
Art	Large patches	Field 9 points/quadra	90
Ely	Small patches	Field 1 point/quadra	30
Ota	Small patches	Field 1 point/quadra	30
MDS	Spatially homogeneous	Field 1 point/quadra	30 (IFS) 30 (EFS)
GDS	Spatially homogeneous	Field 1 point/quadra	30
SPV	Very Small patches High intra-pixel diversity	Airborne Mask extraction	176
GDV	Very Small patches High intra-pixel diversity	Airborne Mask extraction	203
Pin	Height >1 m	Airborne Mask extraction	159

3. Materials and Methods

3.1. Airborne Hyperspectral Data

On 18 June 2019, the 18 km coastline of the study site was flown over by a Chieftain PA31-350 aircraft from PIPER (Vero Beach, FL, USA) operated by PIXAIR company, equipped with a Visible Near InfraRed (VNIR) hyperspectral HySpex VNIR 1600 camera from Norsk Elektro Optikk, Skedsmokorset,

Norway, operated by the Laboratory of Planetology and Geodynamics (LPG) and measuring 160 spectral channels (from 409.23 nm to 987.08 nm in steps of 3.61 nm, with a 4.5 nm spectral resolution) and an angle of aperture of 17°. The record of the aircraft attitude, with the fast inertia measurement unit (IMU), coupled to the accurate global positioning system (GPS) of POS AV AP50 OEM (IMU-8) from Applanix (Richmond Hill, Ontario, Canada) mounted in the dual wavelength Ligth Detection and Ranging (LiDAR) Titan of Teledyne Optech Incorporated (Vaughan, Ontario, Canada) was provide by the LiDAR Nantes-Rennes university platform, and the trajectory was calculated by GEOFIT Expert Company (Nantes, France). The images acquired by the VNIR camera were transformed into luminance from a sensor factory calibration and were georeferenced using the airborne trajectory with Airborne Optical Scanner Data (PARGE) v3.4 software (ReSe Applications LLC, Wil, Switzerland) [48]. The overlap between each image was 45% to avoid gaps between irregular flight lines, but only the pixels with the best angle of incidence were kept to minimize the directional effect, as discussed in [48]. Moreover, as discussed in [49], this also minimizes the strong deviations induced by the different spatial resolutions and the distances to the target between field measurements and remote acquisitions [50,51]. Atmospheric corrections were then applied with Atmospheric and Topographic Correction (ATCOR-4) v7.3 software (ReSe Applications LLC, Wil, Switzerland) [48] in order to obtain a VNIR image with a resolution of 1 × 1 m. Using the ASD FieldSpec3 FR spectrometer (Malvern Panalytical Ltd., Royston, UK) of the LPG laboratory, a final spectral intensity adjustment was applied to insure the best matching between airborne and a single ground reflectance of dry sand, removing the weak anomalous spectral undulation that remained after the atmospheric compensation [52].

3.2. UAV Data

On 19 June 2019, a UAV survey covering 4 km of beach dune system at Truc Vert beach was conducted with a DJI Phantom 4 Pro quadricopter, equipped with a 20 MPix camera. Photogrammetry algorithms from the Agisoft Metashape software v1.5, together with the presence of 36 adequately distributed permanent ground control points, allowed generating of a 0.02 m resolution orthomosaic, with a planimetric error of 0.019 m and 0.026 m for the x axis and y axis, respectively [36]. Based on the primary authors expertise on photointerpretation of existing cover types from UAV imagery, the georeferenced orthomosaic was used to generate a suite of masks that allowed extracting control points from airborne VNIR images. A total of 1488 control points (ranging from 63 to 203 per class) were used to generate validation points in order to assess the performances of supervised classification. For only three classes (GDV, Pin, and SPV), control points also allowed the extraction of random training points, which are independent of validation points. First, dense and extensive areas associated with the 11 ground cover types were visually located and digitized on the orthomosaic. These masks were then used to extract the control points from the airborne VNIR image (Figure 2).

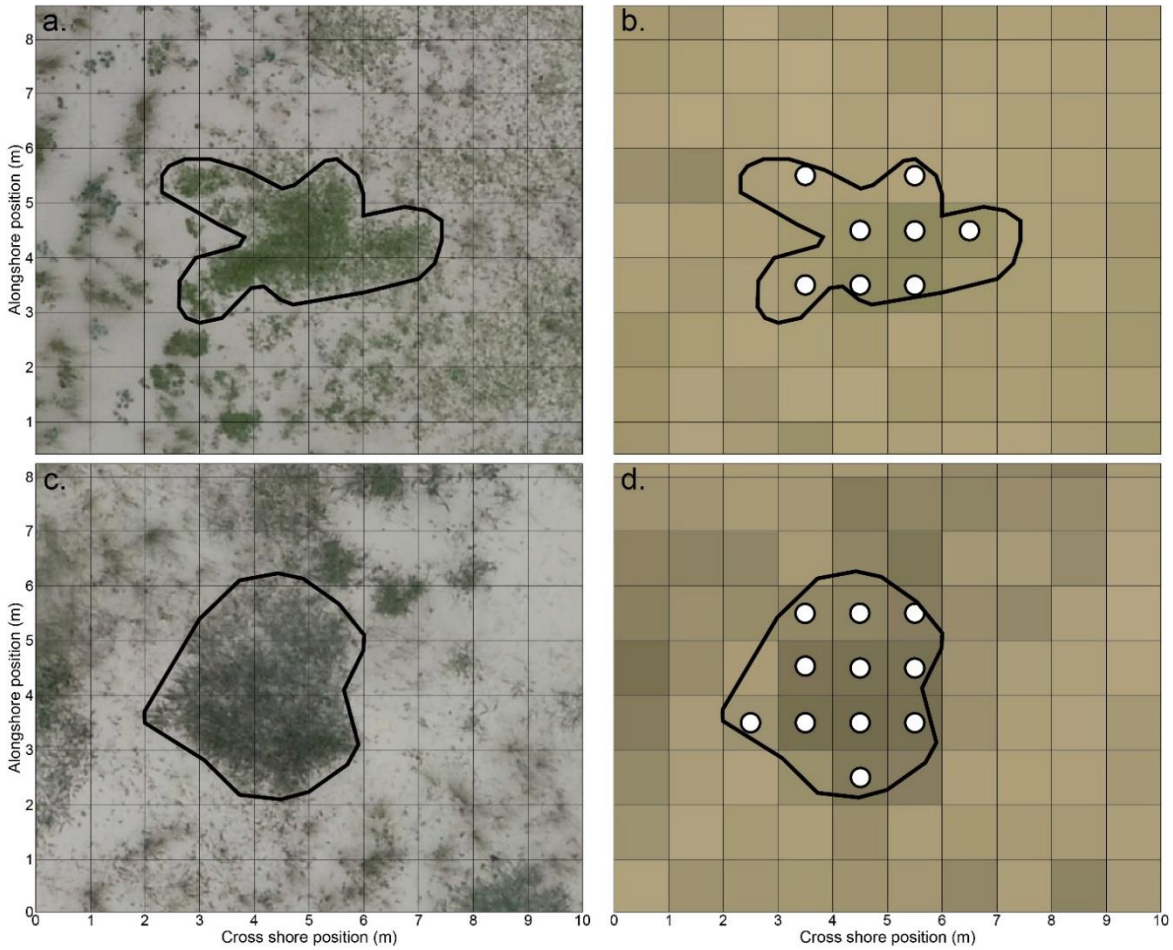

Figure 2. Zoom in on a *Galium arenarium* patch using (**a**) a 0.02 m resolution unmanned aerial vehicle (UAV) orthomosaic and (**b**) a 1 m resolution airbornepseudo-color VNIR image. Zoom in on an *Artemisia campestris* patch using (**c**) an UAV orthomosaic and (**d**) an airborne image. The black lines represent the contour of the vegetation patch, and the white dots the pixels are used as control points.

3.3. Ground Hyperspectral Data

On 25 June 2019, a radiometric ground survey was carried out at Truc Vert beach in order to collect the in situ remote sensing reflectance spectra of different coastal dune cover types. Hyperspectral measurements were performed in the 400–900 nm spectral range (every 3 nanometers) from two radiometrically-calibrated TriOS-RAMSES sensors [53]. The radiance sensor was pointed downward to measure the upward signal of the substrate ($L_u(\lambda)$, $W{\cdot}m^{-2}{\cdot}sr^{-1}{\cdot}nm^{-1}$), while the irradiance sensor was pointed upward to measure the downward irradiance (E_d (λ), $W{\cdot}m^{-2}{\cdot}nm^{-1}$). The radiance sensor had a field of view of 7°. It was mounted on a tripod 1.2 m above the ground (Figure 3a) and provided field samples with a unit area of 0.017 m^2. Radiance and irradiance measurements were performed simultaneously, as in [54]. The remote sensing reflectance ($R_{rs}(\lambda)$, sr^{-1}) was then calculated as the ratio of $L_u(\lambda)$ to $E_d(\lambda)$. Note that, for brevity, hereafter, we did not include the reference to the spectral dependency.

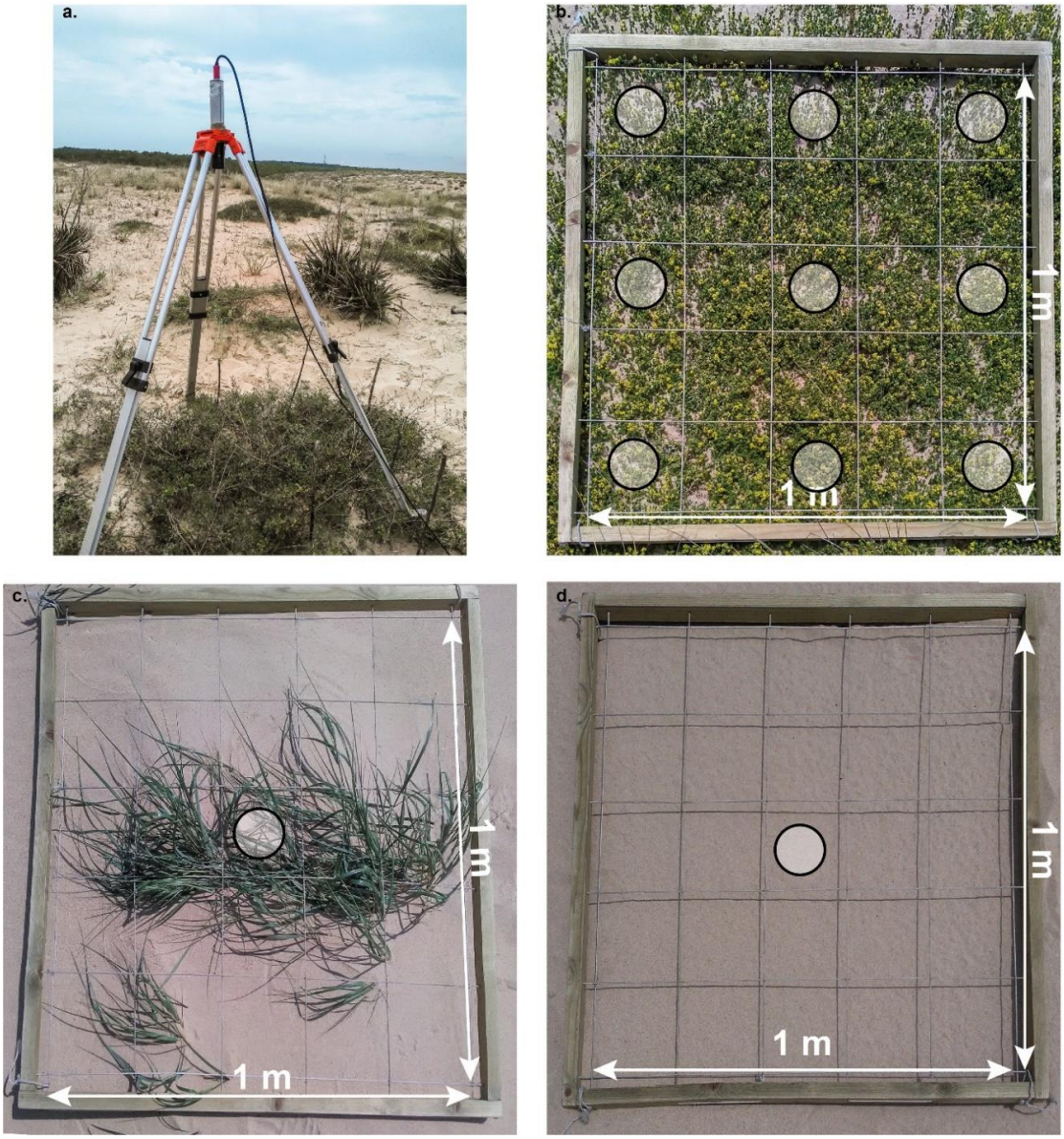

Figure 3. Photos taken at the study site on 25 June 2019, showing (**a**) the deployment mode of radiance TriOS-RAMSES sensor on tripod 1.2 m and the heterogeneity of the optical signal of vegetation and sand covers over unit area of 1 m^2, requiring an adaptive sampling strategy for (**b**) large vegetation patches (example of *Galium arenarium*); (**c**) plant species with isolated individuals, or sparse cover (example of *Elymus farctus*); (**d**) bare dune sand (example of the mobile sand dune).

In complex and very fine-scale fragmented vegetation mosaics, due to a high intra-patch variability of density and vegetation cover, ground R_{rs} spectra are the result of a linear spectral mixture between plant species and soil contributions. Sampling strategies and the number of collected points, summarized in Table 1, were designed to collect the ground reference R_{rs} spectra ($R_{G\text{-}REF}$) of each plant species and sand types with the lowest mixing percentage. Ground measurements were performed in 1 × 1 m^2 representative field sites, dominated by one ground cover type. For plant species with patches equal to or larger than 1 m^2 (Amm, Gal, Hel, Art), a 1 × 1 m^2 quadra was used to collect R_{rs} at nine points homogeneously distributed over features with dense cover (Figure 3b). For plant species characterized by isolated individuals or patches with sparse vegetation covers (Ota and Ely) and for sand types (IFS, EFS, and GDS), three replicates of R_{rs} measurements were performed on individuals,

showing the highest vegetation cover (Figure 2c), and on spatially homogeneous sites (Figure 3d), respectively. Then, for each ground cover type, $R_{\text{G-REF}}$ was computed by averaging all R_{rs} spectra.

It is important to note that no field measurements were performed for SPV, GDV, or Pin. SPV and GDV habitats were characterized by a high spatial variability of intra-patch diversity, which was difficult to record. In addition, the instruments were not suitable to measure Pin species reflectance, due to their height (>2 m).

Associated with radiometric measurements, geo-positioning data, using a differential global navigation satellite system (DGNSS), were collected in order to generate matchups for comparison between ground and airborne hyperspectral data. Finally, a linear interpolation was applied to field data in order to make them compatible with the spectral bands of airborne data.

3.4. Pixel-Based Classification

3.4.1. End-Member Spectra

End-member spectra, associated with the 11 vegetation and sand cover classes, were generated from airborne VNIR training points. For SPV, GDV, and Pin habitats, 50 R_{rs} spectra per ground cover type were randomly extracted from the control points associated with their respective masks. For other types of ground cover, methodology was based on the extraction of 3 × 3 sub-images centered on field measurement locations. These sub-images allowed us to compute for each ground cover type the mean R_{rs} spectra, so called here, the airborne reference R_{rs} spectra ($R_{\text{A-REF}}$), and the airborne reference standard deviation. The analysis of the spectra extracted from control points shows that the spectral variability of R_{rs} for MDS, Ely, Amm, Gal, and Art follows a normal distribution for any wavelengths (p-value of the Shapiro–Wilk normality test <0.01). For GDS, Ota, and Hel, the normality is rejected only for near-infrared (NIR) bands at the 0.01 level but is accepted at the 0.001 level. Based on these results, 50 R_{rs} spectra per ground cover type were further randomly computed using a normal probability law in order to generate the training dataset. In order to take into account all the cross-shore variability associated with MDS, this class was specifically composed of 25 spectra of IFS and 25 spectra of EFS. In total, the vegetation and sand reference dataset consisted of 550 spectra. This procedure allowed reproducing of a spectral mixing range statistically representative of the study site.

The mixing percentage, α, ranging from 0 to 1, could be derived from the linear spectral mixture model:

$$R_{mod} = \alpha \times R_{G-REF;Sdi} + (1 - \alpha) \times R_{G-REF;Spj} \quad (1)$$

where R_{mod} is the modeled R_{rs}, $R_{G\text{-}REF;Sdi}$ is the ground reference R_{rs} spectrum of sand type i, and $R_{G\text{-}REF;Spj}$ isthe ground reference R_{rs} spectrum of plant species j. A root mean square cost function between airborne R_{rs} and R_{mod} was implemented to estimate α values and then its statistical distribution was generated for each plant species.

3.4.2. Normalized Difference Vegetation Index Filter

Prior to applying a supervised classification of the airborne VNIR image, we conducted a first experiment using a spectral index in order to differentiate pixels with and without vegetation covers. This first step was crucial in sparse and very fine-scale fragmented vegetation mosaics. In 1 × 1 m^2 pixels with a low but ecologically significant presence of vegetation, the percentage of sand contribution in the mixing R_{rs} spectrum can be high and may generate misclassified points between vegetation and sand. The normalized difference vegetation index (NDVI) has been proven to be useful for ground cover type characterization [55–57], including, more specifically, coastal dune areas [24]. The NDVI was computed as:

$$\text{NDVI} = \frac{R_{\text{rs}}(\lambda_{\text{NIR}}) - R_{\text{rs}}(\lambda_{\text{R}})}{R_{\text{rs}}(\lambda_{\text{NIR}}) + R_{\text{rs}}(\lambda_{\text{R}})} \quad (2)$$

where the subscripts NIR and R are associated with the near-infrared and red bands, respectively. The differentiating procedure of sand and vegetation covers is based on a NDVI threshold value. The most relevant value was objectively determined using a statistical analysis on the end-member NDVI values.

3.4.3. Random Forest

After having separated the observations into two separate classes (sand or vegetation cover) based on the NDVI index, a Random Forest (RF) classifier [58] was considered for pixel-based classification, as shown in Figure 4. RF is a suitable algorithm for coastal vegetation classification, because of its stability and ability to discriminate ground cover differences [24,32,54,59,60]. When applying the RF classifier, the classification map is accompanied by an accuracy map, which contains the indicator of the confidence degree of the classification. More precisely, the RF classifier is composed of a set of different individual base classifiers (decision trees), each tree giving a decision, and the final decision corresponds to the majority vote. The degree of confidence is obtained as the percentage of individual classifiers that provided a decision equal to the final one.

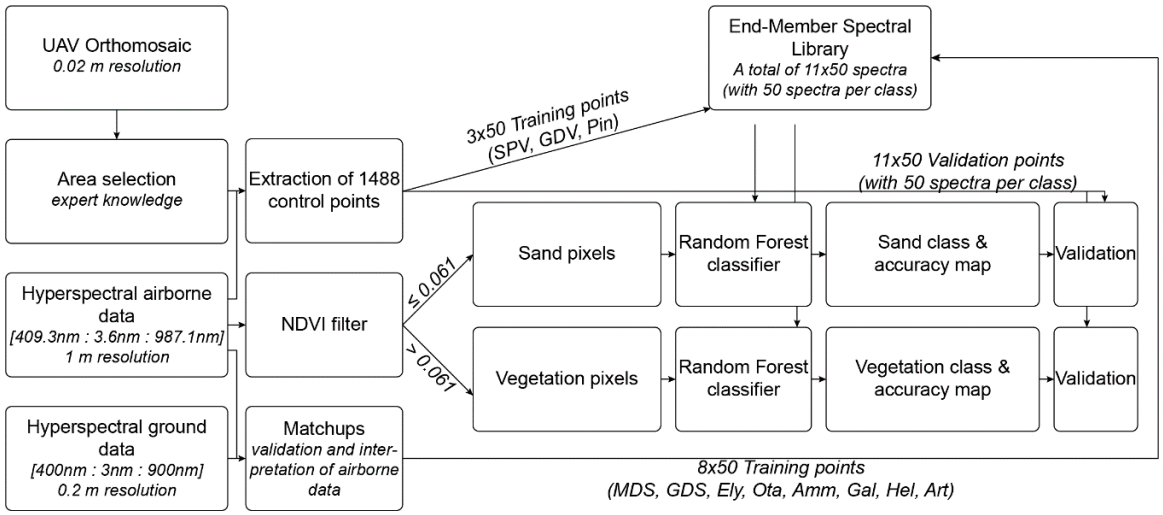

Figure 4. Flow chart depicting the different steps employed in the airborne VNIR image classification.

An accuracy assessment was performed through the confusion matrix, with dimensions equal to the number of classes, from which the overall accuracy was extracted. The agreement between classified points and ground truth was based on a dataset of 550 validation points, i.e., 50 validation points were randomly extracted for each of the 11 cover masks. For SPV, GDV, and Pin vegetation, we removed training points prior to the extraction of validation points.

For SPV, GDV, and Pin vegetation, we removed training points prior to the extraction of validation points. Validation points, training points, and mean ground hyperspectral reflectance spectra are freely available at the Supplementary Materials.

3.5. Stability Index

Based on seasonal surveys of vegetation abundance at this coastal dune system, [40] showed that plant species were spread out according to their tolerance to disturbance, which, in this system, is primarily driven by sand burial. This distribution can be seen in Figure A1 in the correspondence analysis (CA), where plant species have a perfect cross shore distribution along the first axis, representing a disturbance gradient, going from the most disturbed habitat (incipient foredune) to the most stable one (grey dune). Thus, it is possible to extract the CA axis 1 coordinate of each plant species and to associate a value between 0 (highly disturbed) and 1 (highly stable). A value of 0 was associated to the bare sand (MDS and GDS), 1 to Pins and the value of SPV and GDV corresponded to the mean axis

value of species representing theses classes (i.e., *Euphorbia paralias* and *Eryngium maritimum* for SPV and *Phleum arenarium*, *Cerastium glomeratum*, *Corynephorus canescens*, *Vulpia membranacea*, and *Senecio vulgaris* for GDV) (Table 2), calculating a mean stability index for each cross shore transect.

Table 2. Coordinate of each class on the first axis of the correspondence analysis and their associated stability index.

Class	Axis 1 Value [40]	Stability Index
MDS	-	0
GDS	-	0
Ely	−1.12	0.20
Ota	−0.83	0.25
SPV	−0.76	0.27
Amm	−0.33	0.35
Gal	0.14	0.43
Art	0.90	0.57
Hel	1.75	0.73
GDV	2.14	0.8
Pin	-	1.0

4. Results

4.1. Analysis of Spectral Signatures of Ground Cover Types

Mean $R_{\text{G-REF}}$ displays sharp spectral characteristics, which allows discriminating the different ground cover types (Figure 5a). The spectral signature of MDS and GDS is monotonically increasing from blue to near-infrared (NIR) wavelengths. For any spectral bands, GDS shows lower R_{rs} values than MDS, due to the presence of high concentrations of black organic debris strongly absorbing the incident irradiance. $R_{\text{G-REF}}$ spectra of Ely, Gal, and Art show a typical spectral behavior of plant covers with a minimum value at 680 nm and a sharp increase in reflectance values in the red edge region (680–750 nm), due to leaf pigment absorption in red and leaf cellular scattering in NIR spectral bands, respectively [30]. For Ota, Amm, and Hel, $R_{\text{G-REF}}$ spectra are the result of the spectral mixture between sand and plant species. The sand percentage is higher for Ota, which has very scattered patches. It is weaker for Hel. The sampled features have very sharp outlines and are very dense. However, their feature surface is less than 1 m^2, and two of the nine sampled pixels are dominated by GDS cover.

Field and airborne hyperspectral data show good agreement, except for Gal and Art. IFS and EFS, which are characterized by a high optical homogeneity of the substrate into the 3 × 3 box, have the lowest mean relative difference (MRD), with a value of 1.0% and 3.7%, respectively (Figure 5b). Spectral agreement is better for visible wavelengths (0.8% and 1.4% for IFS and EFS, respectively) than for NIR bands (1.3% and 6.9%). GDS, Amm, and Hel, which are characterized by a slight heterogeneity into the 3 × 3 box, have MRD values of 6.3%, 9.9%, and 7.5%, respectively (Figure 5c–e). On the other hand, field and airborne R_{rs} spectra of Gal and Art are significantly different in magnitude, with MRD values of 57.7% and 92.5%, respectively. These differences are due to the non-alignment between airborne grid and field quadrats. While field measurements recorded R_{rs} over dense and homogeneous plant features, airborne measurements recorded R_{rs} of ground covers composed of sand and vegetation. The mixing percentages (see Equation (2)) associated with the Gal and Art $R_{\text{A-REF}}$ are estimated to 51% (MRD = 3.5%) and 46% (MRD = 2%), respectively.

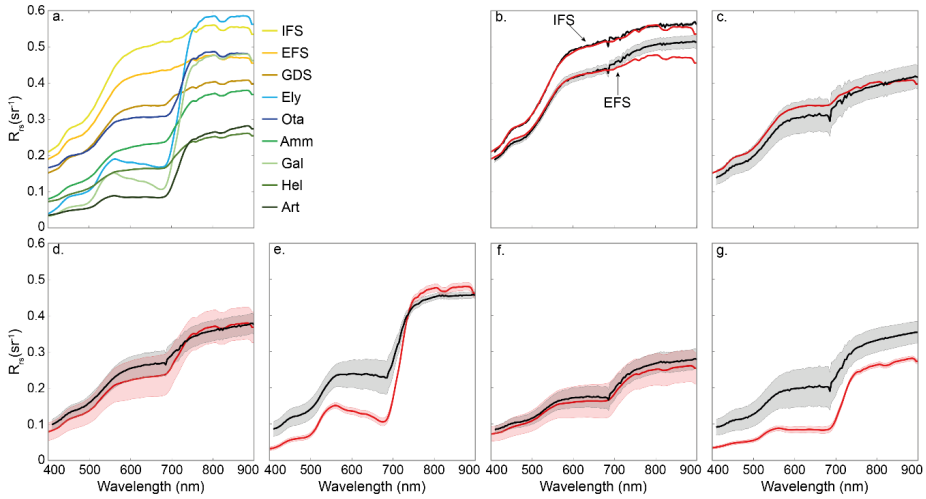

Figure 5. (**a**) Mean ground reference R_{rs} spectra ($R_{G\text{-}REF}$) and comparison with mean airborne reference R_{rs} spectra ($R_{A\text{-}REF}$) for (**b**) incipient foredune sands (IFS) and established foredune sands (EFS), which compose mobile dune sand (MDS), (**c**) GDS, (**d**) *Ammophila arenaria* (Amm), (**e**) *Galium arenarium* (Gal), (**f**) *Helychrisum stoechas* (Hel), and (**g**) *Artemisia campestris* (Art) covers. Black and red lines are associated with $R_{A\text{-}REF}$ and $R_{G\text{-}REF}$, respectively. Grey and red areas correspond to the 95% confidence interval of $R_{A\text{-}REF}$ and $R_{G\text{-}REF}$, respectively. For field data, an up-scaling procedure [61] was used to convert field variance into equivalent airborne variance.

R_{rs} spectra of sand ground covers (Figure 6a,b) display a high spectral variability, which takes into account the cross-shore variability of sand and the variability of black organic debris concentration for MDS and GDS, respectively. Spectral characteristics of plant ground cover R_{rs} of established foredunes and transition dunes show a high mixing percentage with sand. High similarity is observed between Ely (Figure 6c), Ota (Figure 6d), SPV (Figure 6e), and MDS spectra and Amm (Figure 6f), Hel (Figure 6h), and GDS spectra, respectively. On the other hand, R_{rs} spectra of GDV and Pin classes show spectral signatures significantly different than R_{rs} spectra of sand classes. The spectral similarity between some mixed plant species and sand classes can generate misclassified pixels, which impact the performance of supervised classifications. Prior to applying supervised classifications, NDVI was used to differentiate sand and plant ground covers. Several combinations of spectral bands were tested, and the best results were achieved using the red edge bands of 680 nm and 750 nm. Figure 7 shows statistics of NDVI values for the 11 ground cover classes. The first, second, and third quartiles of MDS and GDS were 0.019, 0.025, 0.038, and 0.038, 0.049, 0.061, respectively, while they were 0.066, 0.074, 0.081 for Hel, which displayed the lowest difference. A nonparametric one-way analysis of variance (Kruskal–Wallis test), followed by nonparametric pair-wise comparisons (Wilcoxon–Mann–Whitney test), highlights that NDVI median values between sand and plant species classes are statistically different (p-value ≤ 0.001). Based on the analysis of the NDVI value distribution of GDS and Hel, we selected the threshold value of 0.061 to differentiate sand and plant ground covers. The choice of the third quartile of GDS NDVI values allows to classify sparse vegetation covers as vegetation (see Figure A2 for the NDVI map).

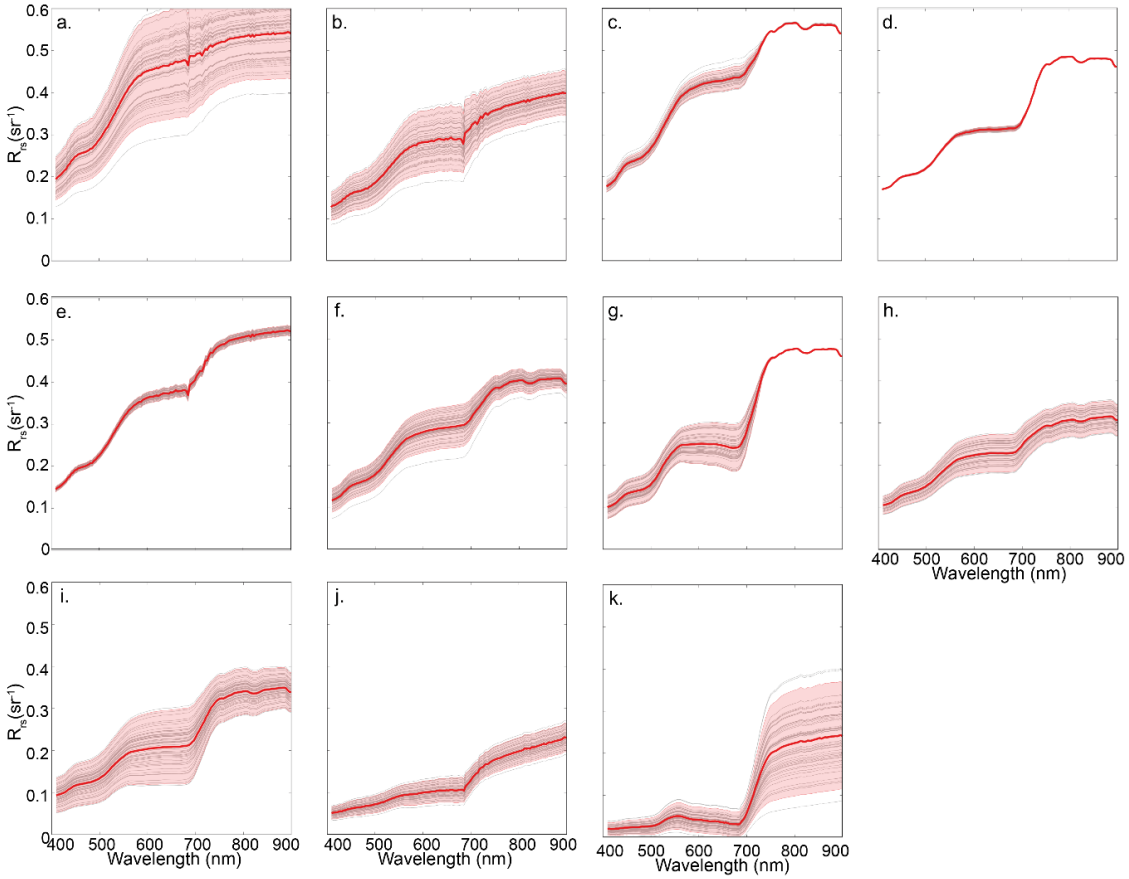

Figure 6. End-member spectra of 11 coastal dune ground cover classes generated from airborne hyperspectral data: (**a**) mobile dune sand (MDS), (**b**) grey dune sand (GDS), (**c**) *Elymus farctus* (Ely), (**d**) *Otanthus* maritimus (Ota), (**e**) sparse vegetation (SPV), (**f**) *Ammophila arenaria* (Amm), (**g**) *Galium arenarium* (Gal), (**h**) *Helychrisum stoechas* (Hel), (**i**) *Artemisia campestris* (Hel), (**j**) grey dune vegetation (GDV), and (**k**) *Pinus marimima* (Pin).

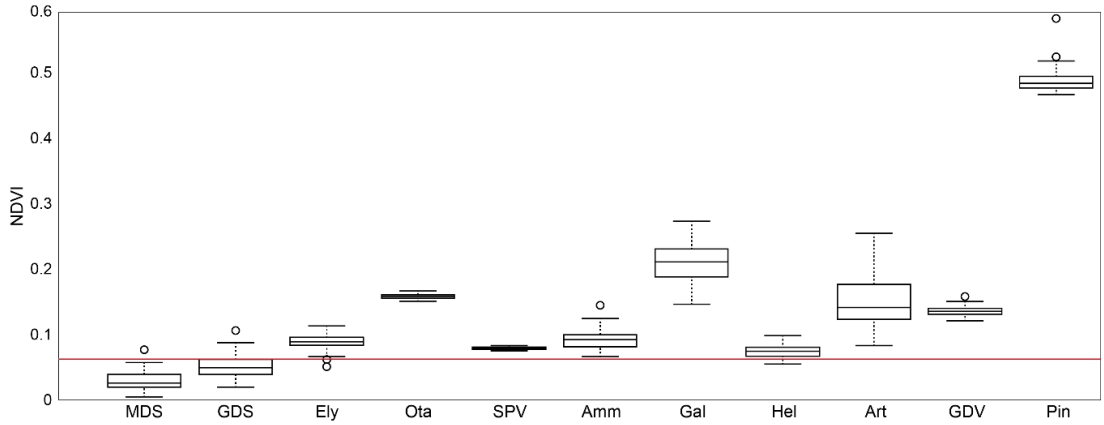

Figure 7. Boxplot of normalized difference vegetation index (NDVI) computed with red edge spectral bands. Within the boxes, bold lines represent median and lower and upper hinges represent first and third quartiles. At the maximum, bars correspond to 1.5 times the interquartile distance and solid circles correspond to observations outside the bars. The red line corresponds to the NDVI threshold of 0.061.

4.2. Assessment of Pixel-Based Supervised Classification Performances

The results of the RF classifier on the 550 validation points are shown in Tables 3 and 4 for sand and vegetation classes, respectively. The discretization between the two sand types is excellent, with an overall accuracy of 100% (Table 3). For vegetation, the overall accuracy is 82.67% (Table 4). Only three classes have a precision lower than 90%; Ely (62%), Ota (10%), and Gal (86%). The poor performance for Ota classification can be attributed to a low variability of its spectral signature in the training dataset (see Figure 6d) and a high similarity of R_{rs} spectra with the other plant classes of the established foredune. For example, 32% of misclassified pixels are associated with SPV. In coastal dune environments, Ota population is composed of isolated individuals and patches with sparse vegetation cover. A spatial resolution of 1 m^2 is clearly a major limitation for the identification of scattered plant species with low ground coverage in complex vegetation mosaic systems.

Table 3. Confusion matrix of the Random Forest (RF) classification for the two sand classes.

	MDS	GDS	Class Accuracy (%)
MDS	50	0	100
GDS	0	50	100

Overall accuracy = 100%.

Table 4. Confusion matrix of the first RF classifier for the nine vegetation classes.

	Ely	Ota	SPV	Amm	Gal	Hel	Arm	GDV	Pin	Class Accuracy (%)
Ely	31	0	19	0	0	0	0	0	0	62
Ota	7	5	16	9	9	0	4	0	0	10
SPV	0	0	50	0	0	0	0	0	0	100
Amm	0	0	0	50	0	0	0	0	0	100
Gal	0	0	7	0	43	0	0	0	0	86
Hel	0	0	0	0	0	50	0	0	0	100
Arm	0	0	0	2	0	0	48	0	0	96
GDV	0	0	0	0	0	0	0	50	0	100
Pin	0	0	0	2	0	0	3	0	45	90

Overall accuracy = 82.67%.

Despite an overall accuracy reaching 82.67%, which already represents a good agreement [62], a second RF model was learned by integrating *Otanthus maritimus* in the SPV class (Table 5). For this second RF vegetation classification, Ely and Gal are still under 90% accuracy, with 64% and 82%, respectively. According to the confusion matrix, the misclassified Ely and Gal pixels are in SPV. Indeed, in their undeveloped stage, Ely and Gal are characterized by small plants of about 10 cm and are quite isolated on a surface area of 1 m^2. It is only when they are well developed that they can easily cover this surface and thus be well classified. However, the overall accuracy of the vegetation species classification reaches 92.25%, which represents a strong agreement [62].

The RF classifier also highlights the importance of the spectral channels used in the classification. Thus, it was possible to study the impact of the number of bands used (from the most to the least important) on the overall accuracy of the vegetation classification, which increases non-linearly with the number of channels used (left axis on Figure 8a). In fact, there seems to be a threshold of 19 bands that allows the accuracy to increase from 76.75% (with 18 channels) to 83.5% before asymptotically increasing. This sudden increase in accuracy was obtained by adding the wavelength 675 nm, whereas all the bands used before were between 750 nm and 900 nm, highlighting the importance of NIR wavelengths in the classification of plant species (right axis on Figure 8a). In addition to the spectral resolution, the impact of the spatial resolution on the vegetation classification accuracy was evaluated by progressively degrading the pixel size from 1 m^2 to 20 m^2. Our classification procedure was then applied to the entire image for the eight vegetation classes. The classification accuracy ranged from

92.75% for 1 m^2 pixel to 73.02% for 2 m^2 pixel then decreased drastically below 70% for larger sizes (Figure 8b).

Table 5. Confusion matrix of the second RF classifier for the eight vegetation classes (after merging Ota and SPV).

	Ely	Spv	Amm	Gal	Hel	Arm	GDV	Pin	Class Accuracy (%)
Ely	32	18	0	0	0	0	0	0	64
Spv	0	50	0	0	0	0	0	0	100
Amm	0	0	50	0	0	0	0	0	100
Gal	0	9	0	41	0	0	0	0	82
Hel	0	0	2	0	48	0	0	0	96
Arm	0	0	0	0	2	48	0	0	96
GDV	0	0	0	0	0	0	50	0	100
Pin	0	0	0	0	0	0	0	50	100

Overall accuracy = 92.25%.

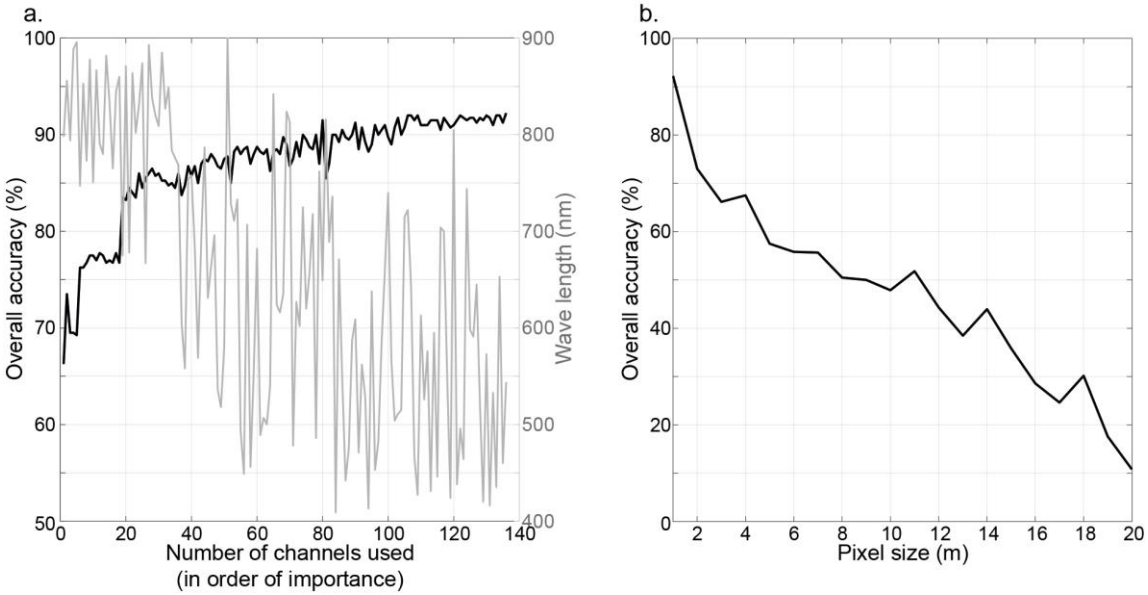

Figure 8. (**a**) Evolution of the overall accuracy (left axis) for the vegetation class and the selected wavelength (right axis) as a function of the number of channels used in the RF classifier (classed in order of importance according to their mean decrease in the Gini index) and (**b**) evolution of the overall accuracy as a function of the pixel size for the vegetation class.

4.3. Spatial Distribution of Coastal Dune Vegetation

The aerial image (Figure 9a) shows a relatively alongshore-uniform coastal dune, which is well vegetated, except at the southern end between −6 and −10 km, characterized by a much less dense and heterogeneous dune vegetation cover and a large bare sand surface. The RF classification map (Figure 9b) shows that each plant species is well classified in its ecosystem (e.g., Ely in incipient foredunes, Amm in established foredunes), with an accuracy generally better than 50% in the transition dune and better than 70% in the other dune units (Figure 9c). The alongshore stability index is in line with visual observation (Figure 9a), with an average value of 0.37 (std = 0.09, se = 7.52×10^{-4}) between the northern limit and −6 km alongshore. Some variations are also locally observed due to the presence of access tracks. In the southern sector, between −6 and −10 km, a high alongshore variability is observed, with a mean stability index of 0.33 (std = 0.15, se = 2.5×10^{-3}) (Figure 9d).

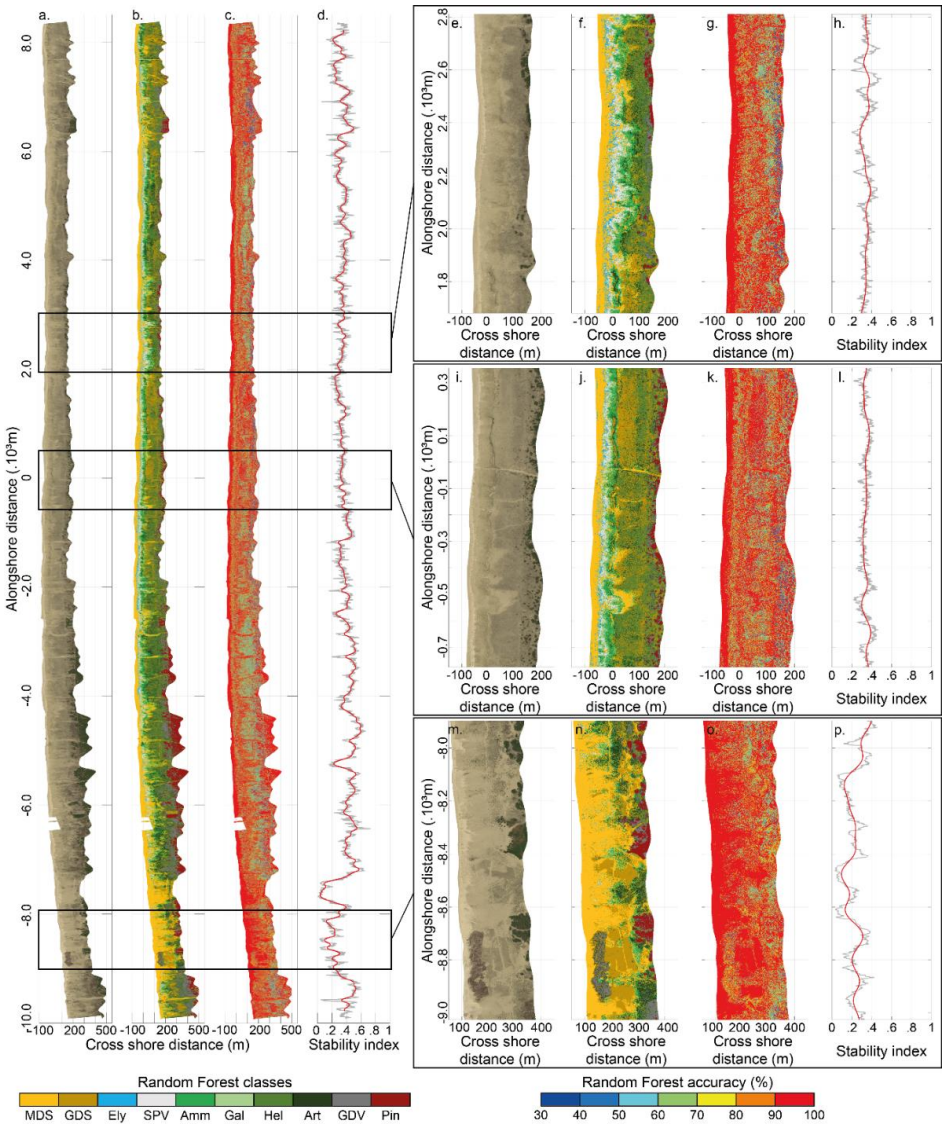

Figure 9. Representation of the 18 km alongshore of the study site with (**a**) the aircraft color orthophoto, (**b**) the result of RF classification, (**c**) the results of RF classification accuracy, and (**d**) the stability index. The right panels represent 1.1 km alongshore zooms of these four parameters for (**e**–**h**) the northern, (**i**–**l**) the central, and (**m**–**p**) the southern zone.

The RF classification also highlights the percentage of appearance of each class (Table 6) with the predominance of the dominant species, such as Amm representing the established foredune (10.64%), Hel representing the transition dune (17.77%), and GDV (7.40%) representing the grey dune. The presence of MDS is generally higher than GDS because of the greater plant cover in the transition dune and grey dune than in the incipient and established foredunes. Only the central area (Figure 9j) shows a lower percentage of MDS than GDS. This can be mainly attributed to a narrower width of the established foredune.

Table 6. Percentage of presence of each class of the different areas of Figure 9.

Class	Overall (%) (Figure 9b)	Southern Area (%) (Figure 9n)	Central Area (%) (Figure 9j)	Northern Area (%) (Figure 9f)
MDS	21.84	41.20	19.12	24.83
GDS	16.16	21.63	22.87	11.27
Ely	2.42	0.34	2.62	4.86
SPV	2.61	0.22	2.99	5.92
Amm	10.64	8.11	9.95	12.22
Gal	3.63	1.82	4.14	5.69
Hel	17.77	3.80	22.66	18.54
Arm	11.44	9.85	7.74	9.51
GDV	7.40	6.05	3.84	4.53
Pin	6.09	6.98	4.07	2.63

The large bare sand areas in the southern area, between −6 km and −10 km, are clearly visible in the 1.1 km alongshore zoom (Figure 9m,n), where they represent 62.83% of the surface. These areas, with a low vegetation cover and quite a low and variable stability index (mean value of 0.23, with std = 0.10, se = 2.9×10^{-3}) characterize a less stable and therefore possibly more mobile sand dune (Figure 9p and Table 6). To limit such dune mobility and prevent blowout development, coastal dune stakeholders have developed various techniques, including the laying of tree branches. This technique, which aims to stop Aeolian erosion and favor sand deposition, is often used to stabilize active dune blowout and/or to protect the inland infrastructures (roads, buildings) or forests from the windblown sand [46,47]. Tree branches within the established foredune are visible in the zoom into the southern zone. Nevertheless, the class associated with this type of cover has not been taken into account in this study due to the low number of control points. As a consequence, tree branch cover is mainly classified as GDV generating misclassified pixels. This class should be taken into account in future research.

The zoom into the northern zone (Figure 9e,f) shows a greater stability, with an average stability index of 0.31 with some alongshore variations (std = 0.06, se = 1.7×10^{-3}) (Figure 9h). Indeed, the established foredune width is not uniform alongshore and shows variations by several tenths of meters in width. Such variability is caused by the localized presence of developing blowouts, leading to the presence of sand deposition fields across the transition dune. In turn, this promotes the presence of vegetation tolerant to physical disturbance (i.e., Ely and SPV) over a large cross-shore distance of about 75 m.

Finally, the zoom on the central area (Figure 9i,j) shows greater stability than the two previous sectors, with an almost alongshore-uniform stability index with an average of 0.36 (std = 0.05, se = 1.6×10^{-3}) (Figure 9i). Plant species characteristics of disturbed environments are present only over a short cross-shore distance of less than 50 m. Moreover, the classification highlights the recolonization of the vegetation of a sand deposition field, extending approximately 100 m in the cross shore direction across the transition dune that formed during the severe 2017–2018 winter storms [36], covering plant species that are not tolerant to sand burial with about 10 cm of sand.

5. Discussion

The first objective of this paper was to develop a pixel-based classification approach in order to generate a comprehensive coastal dune cover mapping, including a large number of classes. Such classes are critical for coastal dune managers in the short term, e.g., to address blowout development or the impact of fencing or branching on vegetation dynamics. In the long-term, for example, decade(s), such mapping will provide new insight into the large-scale variability of vegetation ground cover type in relation to natural (e.g., marine erosion) and anthropogenic (e.g., dune reshaping) forcings. However, a major drawback for remotely sensed application in fragmented and fine-scale environments is the high spectral similarity between different vegetation cover types due to spectral mixing with sand.

To address this issue, recent research has focused on phenology-based [24] or spectral library-based [34] approaches. For high-energy eroding sandy coasts, the high mobility of MDS significantly reduces the interest of the former approach.

Spectral library approaches require specific procedures to generate end members [34,63]. To take into account the range of natural variability of spectral mixing into each class, matchups between ground and airborne data are used to compute airborne reference reflectance spectra ($R_{\text{A-REF}}$) and its standard deviation. The normal probability law is then used to randomly generate end-member spectra of each class. In a pre-analysis, two other procedures were tested using ground reference reflectance spectra ($R_{\text{G-REF}}$) and $R_{\text{A-REF}}$ spectra, respectively. End-member spectra were then modeled using the linear spectral mixture model for different ranges of α values, selected from the statistical analysis of training points. The highest classification performances using RF classifiers were obtained for the procedure described in this paper. The performances of our approach, with an overall accuracy of 92.3% for plant species classes, highlight that the normal probability law procedure is relevant to generate end members representative of the natural variability of spectral mixing into each vegetation cover type.

However, some limitations should be noted. At the dune system scale, the cross-shore distribution of species was in line with the location of their ecological niche. At the community scale, species with dense, large, and well-delimited patches displayed high accuracy (from 96% to 100%), while species with isolated or scattered patches (especially during the early stages of development) showed a lower accuracy (from 64 to 82%). Moreover, if the overall accuracy of SPV and GDV classes reaches 100%, no proportion of the different merged species can be provided. To enhance the monitoring and detection of fragmented and interspersed species, end member spectral libraries should be based on hyperspectral ground data [34,63]. This requires a specific sampling design to match the scale of ground data with that of large-scale observations [63] or to apply up-scaling procedures [61].

The second objective was to characterize the coastal dune stability patterns using sediment and vegetation cover mapping. Results highlight a high spatial variability of the stability index, which can be used to identify areas that may be more vulnerable to the storms. Vulnerability of coastal dunes is often attributed to a lack of vegetation cover, which reduces stability. This was observed in the southern part of the study area. This sector was characterized by a low vegetation cover and wide sand bare surfaces, where the average stability index was only 0.33, whereas it reached an average of 0.37 in the central and northern part, where the vegetation cover was denser, leaving less space for the sand. This methodological approach can become an efficient tool for researchers and coastal dune stakeholders. For instance, the mapping of plant species and sandy areas may allow the monitoring and detection of the different stages of blowout development and detection of the colonization of sandy areas by pioneer species, shrubs, and *Pinus maritima* colonization in the transition dune. However, for specific monitoring of small and sparse plant species, hybrid hyperspectral pixel-based and high resolution object-oriented approaches should be considered, either with coupling of optical satellite missions or with sensors on board UAVs, depending on the surface area to be monitored.

6. Conclusions

Recent technological and methodological advances in remote sensing and mapping tools have greatly facilitated the monitoring of spatiotemporal distribution of vegetation at species and habitat scales. In order to improve our understanding of coastal dune evolution, we developed an original pixel-based classification approach to detect a large range of ground cover classes for environments characterized by fragmented and fine-scale landscape patterns. The development of our classification approach was based on a comprehensive multi-scale dataset combining UAV, hyperspectral ground, and airborne data, collected along a 20-km stretch of a coastal dune system in southwest France. The results showed high classification performances with regard to the large number of cover classes and their low dissimilarities due to high spectral mixing levels. The high performances highlight that the methodology used to generate the end member spectral library meets representativeness

requirements. Additionally, the two-step approach allows us to reduce misclassified pixels. Finally, the stability index mapping, derived from the sediment and vegetation mapping, provides large scale insight into the vulnerability of coastal dunes. We believe that the methodology developed in this paper can become an efficient tool for supporting coastal dune management.

Supplementary Materials: Mean ground hyperspectral reflectance spectra, training dataset, and validation dataset are freely available at http://www.mdpi.com/2072-4292/12/14/2222/s1, The methodology used to compute mean ground hyperspectral reflectance spectra is described Section 3.3. The methodology used to generate training and validation points is described Sections 3.3, 3.4.1 and 3.4.2.

Author Contributions: Conceptualization, B.L., B.C., and R.M.; methodology, B.L., Q.L.-F., and L.B.; software, L.B., B.L., and V.M.; validation, Q.L.-F. and B.L.; formal analysis, Q.L.-F. and B.L.; investigation, Q.L.-F. and B.L.; resources, Q.L.-F., V.M., B.L., P.L., M.G., C.N., and D.R.; data curation, Q.L.-F.; writing—original draft preparation, Q.L.-F. and B.L.; writing—review and editing, Q.L.-F., B.L., B.C., R.M., V.M., L.B., P.L., C.N., and D.R.; visualization, Q.L.-F. and B.L.; supervision, B.L., B.C., and R.M.; project administration, B.C.; funding acquisition, B.C. All authors have read and agreed to the published version of the manuscript.

Funding: This research was funded by Agence National de la Recherche (ANR) grant ANR-14-ASTR-0004 (CHIPO project) and ANR-17-CE01-0014 (SONO project). Additional funding was provided by Service National d'Observation (SNO) Dynalit, labelled by CNRS-INSU, Observatoire Aquitain des Sciences de l'Univers (OASU) and Observatoire de la Côte Aquitaine (OCA). The Nantes Rennes LiDAR platform was funded by the Region Pays de la Loire and the Region Bretagne, with a European Regional Development Fund (ERDF). The LPG hyperspectral camera was funded by the Contrat de Projet Etat Region des Pays de la Loire (CPER R 51_p6 2007–2013) with ERDF funds.

Acknowledgments: Truc Vert is a monitoring site of SNO Dynalit, labelled by CNRS-INSU. Storage resources for this study were provided by the computing facilities MCIA (Mésocentre de Calcul Intensif Aquitain) of Univ. Bordeaux and Univ. Pau et Pays de l'Adour. We thank the RStudio Team (2020). RStudio: Integrated Development Environment for R. RStudio, PBC, Boston, MA, URL http://www.rstudio.com/.

Conflicts of Interest: The authors declare no conflict of interest.

Appendix A

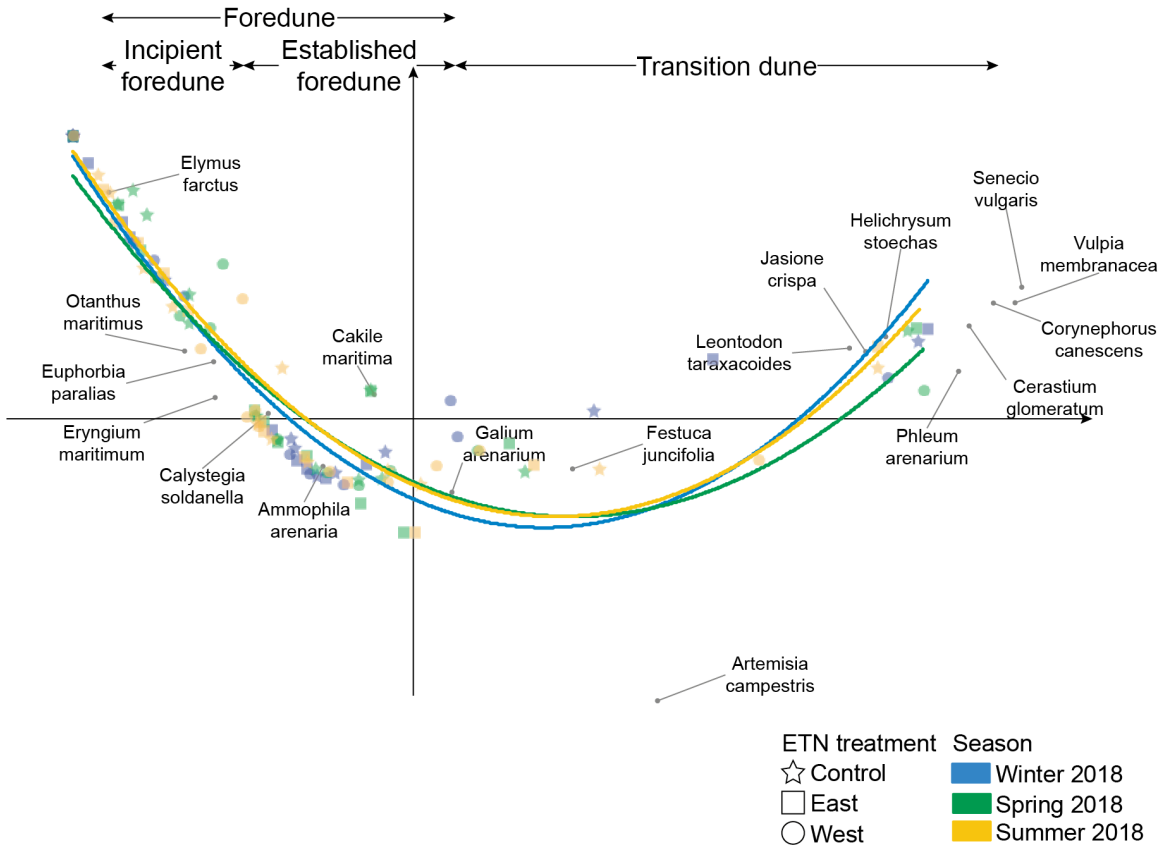

Figure A1. Correspondence analysis 1–2 diagram for vegetation quadrats, where axis 1 plant species coordinates were used to calculate the stability index. Extracted from [40].

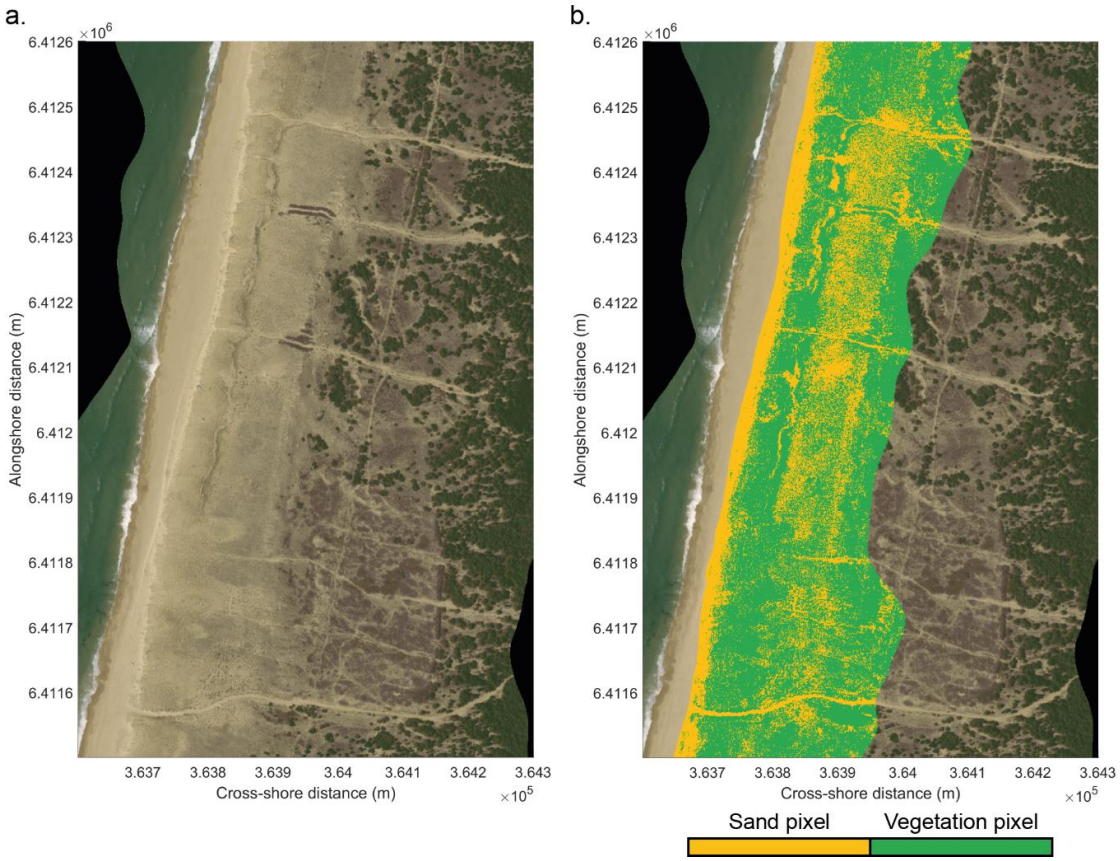

Figure A2. (**a**) Color orthophoto generated by airborne data and (**b**) result of the classification based on NDVI filter to discriminate sand and vegetation covers. The pixels at the western position of the beach—incipient foredune limit and the pixels at the eastern position of the iso contour z = 12 m have been filtered beforehand.

References

1. Swift, D.J.P. Coastal sedimentation. In *Marine Sediment Transport and Environmental Management*; Stanley, D.J., Swift, D.J.P., Eds.; Wiley: New York, NY, USA, 1996; pp. 255–3101.
2. Short, A.D.; Hesp, P.A. Wave, beach and dune interactions in southeastern Australia. *Mar Geol.* **1982**, *48*, 259–284. [CrossRef]
3. Nordstrom, K.F. *Beaches and Dunes of Developed Coasts*; Cambridge University Press: Cambrige, UK, 2000.
4. Hesp, P.A. Foredunes and blowouts: Initiation, geomorphology and dynamics. *Geomorphology* **2002**, *48*, 245–268. [CrossRef]
5. Psuty, N. The coastal foredune: A morphological basis for regional coastal dune development. In *Coastal Dunes*; Martínez, M.L., Psuty, N.P., Eds.; Springer: Berlin, Germany, 2008; Volume 171, pp. 11–27.
6. Zarnetske, P.L.; Hacker, S.D.; Seabloom, E.W.; Ruggiero, P.; Killian, J.R.; Maddux, T.B.; Cox, D. Biophysical feedback mediates effects of invasive grasses on coastal dune shape. *Ecology* **2012**, *93*, 1439–1450. [CrossRef] [PubMed]
7. Hesp, P.A.; Walker, I.J. Aeolian environments: Coastal dunes. In *Treatrise on Geomorphology, Volume 11: Aeolian Geomorphology*; Shroder, J., Lancaster, N., Sherman, D.J., Baas, A.C.W., Eds.; Academic Press: San Diego, CA, USA, 2013; pp. 109–133.
8. Oosting, H. Tolerance to salt spray of plants of coastal dunes. *Ecology* **1945**, *26*, 85–89. [CrossRef]
9. Barbour, M.; Jong, T.; Pavlik, B. Marine beach and dune plant communities. In *Physiological Ecology of North American Plant Communities*; Chabot, B., Mooney, H., Eds.; Chapman & Hall and Methuen: New York, NY, USA, 1985; pp. 296–322.
10. Wilson, J.B.; Sykes, M.T. Is zonation on coastal sand dunes determined primarily by sand burial or by salt spray? A test in New Zealand dunes. *Ecol. Lett.* **1999**, *2*, 233–236. [CrossRef]
11. Houser, C.; Wernette, P.; Rentschlar, E.; Jones, H.; Hammond, B.; Trimble, S. Post-storm beach and dune recovery: Implications for barrier island resilience. *Geomorphology* **2015**, *234*, 54–63. [CrossRef]
12. Martinez, M.L.; Hesp, P.A.; Gallego-Fernandez, J.B. Coastal dunes: Human impact and need for restoration. In *Restoration of Coastal Dunes*; Martinez, M.L., Gallego-Fernández, J.B., Hesp, P., Eds.; Springer: Berlin/Heidelberg, Germany, 2013; pp. 1–14.
13. Bakker, M.A.J.; van Heteren, S.; Vonhogen, L.M.; van der Spek, A.J.F.; van der Valk, B. Recent coastal dune development: Effect of sand nourishments. *J. Coast. Res.* **2012**, *23*, 587–601.
14. Arens, S.M.; Baas, A.C.W.; van Boxel, J.H.; Kaleman, C. Influence of reed stem density on foredune development. *Earth Surf. Process. Landf.* **2001**, *26*, 1161–1176. [CrossRef]
15. Ruz, M.H.; Anthony, E.J. Trapping by brushwood fences on a beach-foredune contact: The primacy of the local sediment budget. *Zeitschrift fur Geomorphol.* **2008**, *52*, 179–194. [CrossRef]
16. Nordstrom, K.F.; Arens, S.M. The role of human actions in evolution and management of foredunes in the Netherlands and New Jersey, USA. *J. Conserv.* **1998**, *4*, 169–180. [CrossRef]
17. Nordstrom, K.F.; Lampe, R.; Vandemark, L.M. Re-shaping naturally-functioning dunes on developed coasts. *Environ. Manag.* **2000**, *25*, 37–51. [CrossRef] [PubMed]
18. Jackson, N.L.; Nordstrom, K.F. Aeolian sediment transport and morphologic change on a managed and an unmanaged foredune. *Earth Surf. Process. Landf.* **2013**, *38*, 413–420. [CrossRef]
19. Castelle, B.; Laporte-Fauret, Q.; Marieu, V.; Michalet, R.; Rosebery, D.; Bujan, S.; Lubac, B.; Bernard, J.-B.; Valance, A.; Dupont, P.; et al. Nature-Based Solution along High-Energy Eroding Sandy Coasts: Preliminary Tests on the Reinstatement of Natural Dynamics in Reprofiled Coastal Dunes. *Water* **2019**, *11*, 2518. [CrossRef]
20. Durán, O.; Moore, L.J. Vegetation controls on the maximum size of coastal dunes. *Proc. Natl. Acad. Sci. USA* **2013**, *110*, 17217–17222. [CrossRef] [PubMed]
21. Seabloom, E.W.; Ruggiero, P.; Hacker, S.D.; Mull, J.; Zarnetske, P. Invasive grasses, climate change, and exposure to storm-wave overtopping in coastal dune ecosystems. *Glob. Chang. Biol* **2013**, *19*, 824–832. [CrossRef]
22. Psuty, N.P.; Silveira, T.M. Global climate change: An opportunity for coastal dunes? *J. Coast. Conserv.* **2010**, *14*, 153–160. [CrossRef]
23. Adam, E.; Mutanga, O.; Rugege, D. Multispectral and hyperspectral remote sensing for identification and mapping of wetland vegetation: A review. *Wetlands Ecol. Manag.* **2010**, *18*, 281–296. [CrossRef]

24. Marzialetti, F.; Giulio, S.; Malavasi, M.; Sperandii, M.G.; Rosario Acosta, A.T.; Carranza, M.L. Capturing coastal dune natural vegetation types using a phenology-based mapping approach: The potential of Sentinel-2. *Remote Sens.* **2019**, *11*, 1506. [CrossRef]
25. De Giglio, M.; Greggio, N.; Goffo, F.; Merloni, N.; Dubbini, M.; Barbarella, M. Comparison of pixel- and object-based classification methods of unmanned aerial vehicle data applied to coastal dune vegetation communities: Casal borsetti case study. *Remote Sens.* **2019**, *11*, 1416. [CrossRef]
26. Lawley, V.; Lewis, M.; Clarke, K.; Ostendorf, B. Site-based and remote sensing methods for monitoring indicators of vegetation condition: An Australian review. *Ecol. Indic.* **2016**, *60*, 1273–1283. [CrossRef]
27. Valentini, E.; Taramelli, A.; Cappucci, S.; Filipponi, F.; Nguyen Xuan, A. Exploring the Dunes: The Correlations between Vegetation Cover Pattern and Morphology for Sediment Retention Assessment Using Airborne Multisensor Acquisition. *Remote Sens.* **2020**, *12*, 1229. [CrossRef]
28. Rapinel, S.; Clément, B.; Magnanon, S.; Sellin, V.; Hubert-Moy, L. Identification and mapping of natural vegetation on a coastal site using a Worldview-2 satellite image. *J. Environ. Manag.* **2014**, *144*, 236–246. [CrossRef] [PubMed]
29. Medina Machín, A.; Marcello, J.; Hernández-Cordero, A.I.; Martín Abasolo, J.; Eugenio, F. Vegetation species mapping in a coastal-dune ecosystem using high resolution satellite imagery. *GISci. Remote Sens.* **2019**, *56*, 210–232. [CrossRef]
30. Hennessy, A.; Clarke, K.; Lewis, M. Hyperspectral Classification of Plants: A Review of Waveband Selection Generalisability. *Remote Sens.* **2020**, *12*, 113. [CrossRef]
31. Filippi, A.M.; Jensen, J.R. Fuzzy learning vector quantization for hyperspectral coastal vegetation classification. *Remote Sens. Environ.* **2006**, *100*, 512–530. [CrossRef]
32. Timm, B.C.; McGarigal, K. Fine-scale remotely-sensed cover mapping of coastal dune and salt marsh ecosystems at Cape Cod National Seashore using Random Forests. *Remote Sens. Environ.* **2012**, *127*, 106–117. [CrossRef]
33. Schmidt, K.S.; Skidmore, A.K. Spectral discrimination of vegetation types in a coastal wetland. *Remote Sens. Environ.* **2003**, *85*, 92–108. [CrossRef]
34. Marcos Jiménez, M.; Díaz-Delgado, R. Towards a standard plant species spectral library protocol for vegetation mapping: A case study in the shrubland of Doñana National Park. *ISPRS Int. J. Geoinf.* **2015**, *4*, 2472–2495. [CrossRef]
35. Castelle, B.; Bujan, S.; Ferreira, S.; Dodet, G. Foredune morphological changes and beach recovery from the extreme 2013/2014 winter at a high-energy sandy coast. *Mar. Geol.* **2017**, *385*, 41–55. [CrossRef]
36. Laporte-Fauret, Q.; Marieu, V.; Castelle, B.; Michalet, R.; Bujan, S.; Rosebery, D. Low-Cost UAV for high-resolution and large-scale coastal dune change monitoring using photogrammetry. *J. Mar. Sci. Eng.* **2019**, *7*, 63. [CrossRef]
37. Forey, E.; Chapelet, B.; Tilquin, M.; Vitasse, Y.; Touzard, B.; Michalet, R. The relative importance of disturbance and environmental stress at local and regional scales in French coastal sand dunes. *J. Veg. Sci.* **2008**, *19*, 493–502. [CrossRef]
38. Forey, E.; Touzard, B.; Michalet, R. Does disturbance drive the collapse of biotic interactions at the severe end of a diversity-biomass gradient? *Plant Ecol.* **2010**, *206*, 287–295. [CrossRef]
39. Le Bagousse-Pinguet, Y.; Forey, E.; Touzard, B.; Michalet, R. Disentangling the effects of water and nutrients for studying the outcome of plant interactions in sand dune ecosystems. *J. Veg. Sci.* **2013**, *24*, 375–383. [CrossRef]
40. Laporte-Fauret, Q.; Alonso Ayuso, A.T.; Rodolfo-Damiano, T.; Marieu, V.; Castelle, B.; Bujan, S.; Rosebery, D.; Michalet, R. The role of physical disturbance for ecosystem functioning in coastal sand dunes. *Sci. Total Environ.* submitted.
41. Castelle, B.; Marieu, V.; Bujan, S.; Splinter, K.D.; Robinet, A.; Sénéchal, N.; Ferreira, S. Impact of the winter 2013–2014 series of severe Western Europe storms on a double-barred sandy coast: Beach and dune erosion and megacusp embayments. *Geomorphology* **2015**, *238*, 135–148. [CrossRef]
42. Castelle, B.; Dodet, G.; Masselink, G.; Scott, T. A new climate index controlling winter wave activity along the Atlantic coast of Europe: The West Europe Pressure Anomaly. *Geophys. Res. Lett.* **2017**, *44*, 1384–1392. [CrossRef]

43. Castelle, B.; Guillot, B.; Marieu, V.; Chaumillon, E.; Hanquiez, V.; Bujan, S.; Poppeschi, C. Spatial and temporal patterns of shoreline change of a 280-km long high-energy disrupted sandy coast from 1950 to 2014: SW France. *Estuar. Coast. Shelf Sci.* **2018**, *200*, 212–223. [CrossRef]
44. Laporte-Fauret, Q.; Castelle, B.; Marieu, V.; Bujan, S.; Michalet, R.; Rosebery, D. Coastal dune morphology evolution combining Lidar and UAV surveys, Truc Vert beach 2011–2019. In *Global Coastal Issues of 2020. Journal of Coastal Research*; Special Issue No. 95; Malvárez, G., Navas, F., Eds.; Coastal Education and Research Foundation, Inc.: Coconut Creek, FL, USA, 2020; pp. 163–167.
45. Robin, N.; Billy, J.; Castelle, B.; Hesp, P.; Nicolae Lerma, A.; Laporte-Fauret, Q.; Marieu, V.; Rosebery, D.; Bujan, S.; Destribats, B.; et al. 150 years of Foredune initiation and evolution driven by human and natural processes. *Geomorphology*, submitted.
46. Barrère, P. Dynamics and management of the coastal dunes of the Landes, Gascony, France. Coastal Dunes: Geomorphology, ecology and management for conservation. In Proceedings of the 3rd European Dune Congress, Galway, Ireland, 17–21 June 1992; Carter, R.W.G., Curtis, T.G.F., Sheehy-Skeffington, M.J., Eds.; pp. 25–32.
47. Prat, M.; Auly, T. L'évolution du littoral médocain à Lacanau. *Sud-Ouest Eur.* **2010**, *29*, 53–64. [CrossRef]
48. Richter, R.D. Atmospheric/Topographic Correction for Airborne Imagery. In *DLR Report*; DLR-IB 565-02/14, 240; DLR: Cologne, Germany, 2014.
49. Combe, J.P.; Launeau, P.; Pinet, P.; Despan, D.; Harris, E.; Ceuleneer, G.; Sotin, C. Mapping of an ophiolite complex by high-resolution visible-infrared spectrometry. *Geochem. Geophys. Geosyst.* **2006**, *7*. [CrossRef]
50. Friedl, M.A.; Davis, F.W.; Michaelsen, J.; Moritz, M.A. Scaling and uncertainty in the relationship between the NDVI and land surface biophysical variables: An analysis using a scene simulation model and data from FIFE. *Remote Sens. Environ.* **1995**, *54*, 233–246. [CrossRef]
51. Chen, J.M. Spatial scaling of a remotely sensed surface parameter by contexture. *Remote Sens. Environ.* **1999**, *69*, 30–42. [CrossRef]
52. Launeau, P.; Kassouk, Z.; Debaine, F.; Roy, R.; Mestayer, P.G.; Boulet, C.; Rouaud, J.-M.; Giraud, M. Airborne hyperspectral mapping of trees in an urban area. *Int. J. Remote Sens.* **2017**, *38*, 1277–1311. [CrossRef]
53. Hommersom, A.; Kratzer, S.; Laanen, M.; Ansko, I.; Ligi, M.; Bresciani, M.; Giardino, C.; Beltrán-Abaunza, J.M.; Moore, G.; Wernand, M.; et al. Intercomparison in the field between the new WISP-3 and other radiometers (TriOS Ramses, ASD FieldSpec, and TACCS). *J. Appl. Remote Sens.* **2012**, *6*, 063615. [CrossRef]
54. Proença, B.; Frappart, F.; Lubac, B.; Marieu, V.; Ygorra, B.; Bombrun, L.; Michalet, R.; Sottolichio, A. Potential of High-Resolution Pléiades Imagery to Monitor Salt Marsh Evolution After Spartina Invasion. *Remote Sens.* **2019**, *11*, 968. [CrossRef]
55. Tucker, C.J. Red and photographic infrared linear combinations for monitoring vegetation. *Remote Sens. Environ.* **1979**, *8*, 127–150. [CrossRef]
56. Pettorelli, N.; Vik, J.O.; Mysterud, A.; Gaillard, J.-M.; Tucker, C.J.; Stenseth, N.C. Using the satellite-derived NDVI to assess ecological responses to environmental change. *Trends Ecol. Evol.* **2005**, *20*, 503–510. [CrossRef] [PubMed]
57. Verbesselt, J.; Hyndman, R.; Newnham, G.; Culvenor, D. Detecting trend and seasonal changes in satellite image time series. *Remote Sens. Environ.* **2010**, *114*, 106–115. [CrossRef]
58. Breiman, L. Random Forests. *Mach. Learn.* **2001**, *45*, 5–32. [CrossRef]
59. Juel, A.; Groom, G.B.; Svenning, J.C.; Ejrnæs, R. Spatial application of Random Forest models for fine-scale coastal vegetation classification using object based analysis of aerial orthophoto and DEM data. *Int. J. Appl. Earth Observ. Geoinf.* **2015**, *42*, 106–114. [CrossRef]
60. Correll, M.D.; Hantson, W.; Hodgman, T.P.; Cline, B.B.; Elphick, C.S.; Gregory Shriver, W.; Tymkiw, E.L.; Olsen, B.J. Fine-scale mapping of coastal plant communities in the northeastern USA. *Wetlands* **2019**, *39*, 17–28. [CrossRef]
61. Silvestri, S.; Marani, M.; Settle, J.; Benvenuto, F.; Marani, A. Salt marsh vegetation radiometry: Data analysis and scaling. *Remote Sens. Environ.* **2002**, *80*, 473–482. [CrossRef]

62. Foody, G.M. Status of land cover classification accuracy assessment. *Remote Sens. Environ.* **2002**, *80*, 185–201. [CrossRef]
63. Fisk, C.; Clarke, K.D.; Lewis, M.M. Comparison of hyperspectral versus traditional field measurements of fractional ground cover in the Australian arid zone. *Remote Sens.* **2019**, *11*, 2825. [CrossRef]